GEOPHYSICS, VOL. 89, NO. 5 (SEPTEMBER-OCTOBER 2024); P. C211–C223, 13 FIGS., 1 TABLE.
10.1190/GEO2023-0692.1

The qP- and qSV-wave separation in 2D vertically transversely isotropic media and their applications in elastic reverse time migration

Na Fan[1], Xiao-Bi Xie[2], Lian-Feng Zhao[3], and Zhen-Xing Yao[3]

ABSTRACT

Compressional and shear wave separation is an important step in anisotropic elastic reverse time migration (ERTM). With separated wavefields, we can generate images between different wave types and reveal more subsurface physical properties, as well as remove unwanted crosstalk and improve image quality. Traditional Helmholtz decomposition based on divergence and curl operations for isotropic media cannot be directly extended to vertically transversely isotropic (VTI) media. Wave-mode separation methods, similar to the nonstationary spatial filter and Poynting vector, cannot preserve the phase and amplitude information of the original coupled wavefield, thus limiting their application in ERTM. Currently, the anisotropic wavefield decomposition methods include the wavenumber-domain approach, the low-rank approximation, and other separation approaches based on different approximations, e.g., weak or elliptical anisotropy. These methods are either computationally intensive or involve large separation errors, especially in models with strong heterogeneities and anisotropy. The VTI wavefield separation operator is essentially defined in a mixed space-wavenumber domain. We introduce scalar operators to transfer operations from this mixed space-wavenumber domain to the space domain. The local wave propagation direction in the scalar operators is estimated using the Poynting vector, which is highly computationally efficient in the space domain. When we apply the wave separation method to ERTM, we not only obtain the vectorized qP and qSV waves but also retrieve the scalar qP wavefield. The scalar and vector wavefields preserve the amplitude and phase information in the original coupled wavefield. For anisotropic ERTM, we suggest using the scalar imaging condition to generate the PP image and the magnitude- and sign-based vector imaging condition to produce the PS image, both having higher image accuracy than the dot-product imaging condition. Numerical examples are used to validate our anisotropic wavefield separation method and the related ERTM workflow.

INTRODUCTION

Prestack elastic wave reverse time migration (ERTM) is based on the full elastic wave equation. Theoretically, it can accurately handle various wave propagation phenomena, e.g., scattering, reflection, diffraction, and focusing/defocusing in isotropic and anisotropic media (e.g., Baysal et al., 1983; McMechan, 1983; Chang and McMechan, 1987; Xie and Wu, 2005; Sun et al., 2006; Xiao and Leaney, 2010; Du et al., 2017; Zhang et al., 2023). Unlike the acoustic case, ERTM can generate multimode images, such as the PP, PS, SP, and SS composed of more information on the subsurface physical properties. The converted-wave images usually have higher resolution than the pure P-image because the S wave often involves shorter wavelengths (e.g., Yan and Sava, 2008; Yan and Xie, 2012; Du et al., 2014; Shabelansky et al., 2015, 2017).

Subsurface media are generally anisotropic, whereas wave velocities are dependent on the propagation direction (Tsvankin, 2012). Applying isotropic imaging techniques to anisotropic media can cause reduced resolution and inaccurate target positioning. However, research on pure qP wave approximation methods is only

Manuscript received by the Editor 15 November 2023; revised manuscript received 30 May 2024; published ahead of production 26 June 2024; published online 30 August 2024.
[1]Yangtze University, College of Geophysics and Petroleum Resources, Key Laboratory of Exploration Technologies for Oil and Gas Resources of Ministry of Education, Wuhan, China. E-mail: fanna@yangtzeu.edu.cn (corresponding author).
[2]University of California at Santa Cruz, Institute of Geophysics and Planetary Physics, Santa Cruz, California, USA. E-mail: xxie@ucsc.edu.
[3]Chinese Academy of Sciences, Institute of Geology and Geophysics, Key Laboratory of Earth and Planetary Physics, Beijing, China. E-mail: zhaolf@mail.iggcas.ac.cn; yaozx@mail.iggcas.ac.cn.

applicable to traditional 1C imaging and cannot be used for multicomponent imaging (Alkhalifah, 1998; Stovas et al., 2020; Xu et al., 2020; Li and Stovas, 2021; Zhang et al., 2024). Therefore, the development of anisotropic ERTM is important. Among different types of anisotropic models, the vertically transversely isotropic (VTI) model is a commonly used formation. Therefore, in this study, we consider the wavefield separation and ERTM in a 2D VTI medium.

The P- and S-wave separation is a key step in ERTM (e.g., Chang and McMechan, 1987; Sun et al., 2006; Yan and Sava, 2008; Du et al., 2014; Yang et al., 2019). There are two wavefield separation schemes. One is based on the Helmholtz potential (e.g., Dellinger and Etgen, 1990; Yan and Sava, 2009a, 2009b; Zhou and Wang, 2017), in which the phase and amplitude of the separated waves are inconsistent with the original coupled wavefield and must be corrected before applying ERTM (Sun et al., 2001; Sun et al., 2011). Furthermore, the resulting PS image has a polarity reversal at normal incidence, and polarity correction, a complicated and time-consuming process, is required before producing the PS image (Sun and McMechan, 2001; Du et al., 2012; Duan and Sava, 2015). Another separation scheme is based on the vector wavefield decomposition (e.g., Xiao and Leaney, 2010; Zhang and McMechan, 2010; Cheng and Fomel, 2014; Fan et al., 2022). The separated vector P and S waves still preserve the correct phase and amplitude as in the original coupled wavefield. Therefore, this separation scheme is better for ERTM (Du et al., 2014; Zhang and Shi, 2019; Zhou et al., 2019).

In isotropic media, the wavefields are separated by the divergence and curl operators based on Helmholtz's decomposition theorem or by solving the P- and S-wave decoupled elastic wave equations (Xiao and Leaney, 2010; Zhang and McMechan, 2010; Fan et al., 2022). In contrast, the polarizations of P and S waves in anisotropic media are neither parallel nor perpendicular to the wave propagation direction (Tsvankin, 2012). Therefore, the classical Helmholtz theory is invalid. However, the idea of projecting the coupled P and S wavefields onto their polarization directions can be extended to anisotropic media for wave separation. Therefore, the wavefield separation operator for anisotropic media can be constructed from the polarization of qP or qSV waves, and the polarization vectors can be obtained by solving the Christoffel equation (Zhang and McMechan, 2010).

Because the wavefield separation operator for VTI media is defined in the mixed space-wavenumber domain, the easier and more straightforward way is to perform the separation in the wavenumber domain (Zhang and McMechan, 2010). However, although such a scheme works well in a homogeneous medium, it encounters difficulty when we extend it to a heterogeneous medium. If the separation operator is transformed from the wavenumber domain to the space domain with the inverse fast Fourier transform (FFT), similar to the nonstationary spatial filter method (Dellinger and Etgen, 1990; Yan and Sava, 2009a, 2009b), it still faces the problem that it cannot be effectively applied to an inhomogeneous medium. The computational cost will be extremely high, particularly in a 3D heterogeneous medium. A low-rank approximation is another solution to decompose anisotropic wavefields (Cheng and Fomel, 2014; Cheng et al., 2016). It requires multidimensional FFTs that make parallelization inefficient. Subsequently, Wang et al. (2018) propose a localized low-rank approximation, which is performed separately in each divided small block, but intensive FFTs are still required within each small region, and the computational cost is still rather high. There are other separation methods based on different approximations (Yang et al., 2019; Zuo et al., 2022, 2023), but they are often not accurate and only applicable to weak anisotropy. Recently, Zhang et al. (2022) propose an anisotropic Helmholtz wavefield decomposition method in the space-wavenumber domain, but it still requires three FFTs within each time step. To further improve the efficiency, Zhang et al. (2023) develop a fast space-domain anisotropic Helmholtz decomposition method that avoids using multiple FFTs and complex matrix calculations. However, their wavefield separation operators are built based on the approximation around elliptical anisotropy or $\varepsilon = \delta \approx 0$, where ε and δ are the Thomsen anisotropic parameters and have poor performance for models strongly biased from the elliptical anisotropy.

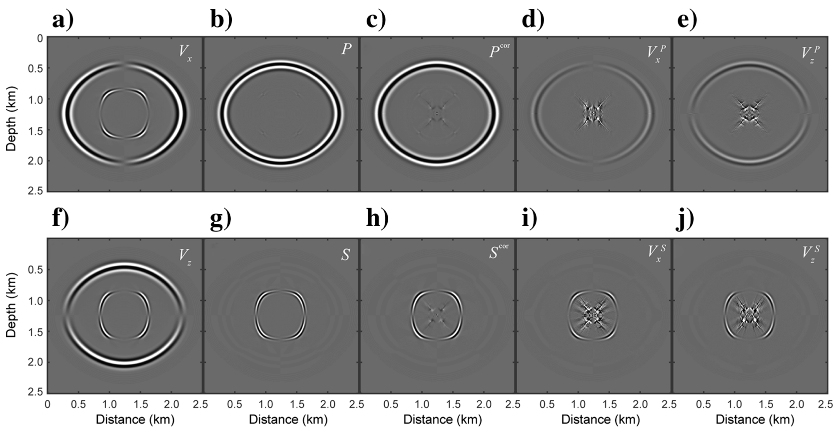

Figure 1. Snapshots for the coupled and separated wavefields calculated using equations 9 and 11 in a homogeneous VTI model. The model parameters are $v_{P0} = 3000$ m/s, $v_{S0} = 1500$ m/s, $\varepsilon = 0.2$, and $\delta = 0.1$. The snapshots are (a) the coupled particle-velocity wavefield in the x-direction V_x; (b) the Helmholtz potential of the qP wave P; (c) the amplitude- and phase-corrected Helmholtz potential of the qP wave or the scalar qP wave P^{cor}; (d and e) the x- and z-components of the separated vector qP wave V_x^P and V_z^P, (f) the coupled particle-velocity wavefield in the z direction V_z; (g) the Helmholtz potential of the qSV wave S; (h) the amplitude- and phase-corrected Helmholtz potential of the qSV wave S^{cor}; and (i and j) the x- and z-components of the separated vector qSV wave V_x^S and V_z^S.

Space-domain separation is usually the most economical algorithm. Zhou and Wang (2017) propose a space-domain method in which the wave propagation direction and polarization direction are calculated using the Poynting vector. Liu et al. (2019) also develop a wave-mode separation method for TI media based on the fast Poynting vector approach. Their methods can separate the qP and qSV wave modes with high precision in the space domain but cannot provide decomposed vectorized wave components. To date, all of the aforementioned vector wave-decomposition methods for anisotropic media, such as the wavenumber-domain approach (Zhang and McMechan, 2010), low-rank approximations (Cheng and Fomel, 2014; Cheng et al., 2016; Wang et al., 2018), and other approaches based on weak or elliptical anisotropy assumptions (Yang et al., 2018; Zuo et al., 2022; 2023; Zhang et al., 2022; 2023), have their advantages and disadvantages. In this study, we introduce a novel anisotropic wavefield decomposition and ERTM method featuring the following innovations:

1) Unlike traditional wave-mode separation methods such as those by Yan and Sava (2009a), Zhou and Wang (2017), and Liu et al. (2019), the proposed vectorized decomposition can preserve the phase and amplitude of the original coupled wavefield.
2) For currently existing vector decomposition methods, those based on a low-rank approximation (Cheng and Fomel, 2014; Cheng et al., 2016) may yield high accuracy but require significant computational resources due to intensive FFTs during each time iteration; others (e.g., Yang et al., 2019; Zuo et al., 2022; 2023; Zhang et al., 2022; 2023) can retain reasonable accuracy only for weak or near-elliptical anisotropic media. Some of these methods (Yang et al., 2019; Zhang et al., 2022; Zuo et al., 2022; 2023) still require intensive FFTs or require solving Poisson's equation. The method by Zhang et al. (2023) stands out for its efficiency but has low accuracy. In this study, we propose a space-domain wavefield decomposition method that has high accuracy, low computational cost, and is suitable for a wide range of anisotropic media.
3) In addition to the commonly generated vectorized qP and qSV waves, the proposed decomposition approach provides a scalar qP wavefield. They all have correct amplitude and phase information. This allows for the possibility of using the scalar imaging condition in anisotropic ERTM.

THEORY

Wavefield separation operator

The qP- and qSV-wave polarization directions can be obtained by solving the Christoffel equation (Tsvankin, 2012). In a 2D VTI medium,

$$\hat{\mathbf{a}}_1 = \begin{bmatrix} k_x \\ \frac{-(c_{11}-c_{44})k_x^2+(c_{33}-c_{44})k_z^2+D_k}{2(c_{13}+c_{44})k_z^2} k_z \end{bmatrix}, \tag{1a}$$

$$\hat{\mathbf{a}}_2 = \begin{bmatrix} k_x \\ \frac{-(c_{11}-c_{44})k_x^2+(c_{33}-c_{44})k_z^2-D_k}{2(c_{13}+c_{44})k_z^2} k_z \end{bmatrix}, \tag{1b}$$

where $\hat{\mathbf{a}}_1$ and $\hat{\mathbf{a}}_2$ are wavenumber-domain polarization vectors of the qP- and qSV-waves, respectively, and $D_k = \sqrt{[(c_{11}-c_{44})k_x^2-(c_{33}-c_{44})k_z^2]^2+4(c_{13}+c_{44})^2k_x^2k_z^2}$. Here, k_x and k_z are wavenumbers in the x- and z-directions, respectively. The term c_{ij} are elements of the VTI stiffness matrix and can be expressed as $c_{11}=(1+2\varepsilon)\rho V_{P0}^2$, $c_{33}=\rho V_{P0}^2$, $c_{44}=\rho V_{S0}^2$, and $c_{13}=\rho\sqrt{[(1+2\delta)V_{P0}^2-V_{S0}^2](V_{P0}^2-V_{S0}^2)}-\rho V_{S0}^2$, where V_{P0} and V_{S0} represent vertical velocities of the qP and qS waves, respectively; ρ is the density; and ε and δ represent the anisotropic parameters (Thomsen, 1986). The detailed derivation of equations 1a and 1b are shown in Appendix A.

Because $\hat{\mathbf{a}}_1$ is perpendicular to $\hat{\mathbf{a}}_2$, we use the qP-wave polarization vector $\hat{\mathbf{a}}_1$ to construct the wavefield separation operator $i\hat{\mathbf{a}}_1$. Because this operator is defined in a mixed space-wavenumber domain and cannot be transformed to the space domain directly, we follow the idea of the scalar operator by Xu and Zhou (2014a, 2014b) and Liang et al. (2023) and let

$$\hat{\mathbf{a}}_1 = \begin{bmatrix} k_x \\ S_k k_z \end{bmatrix}, \tag{2}$$

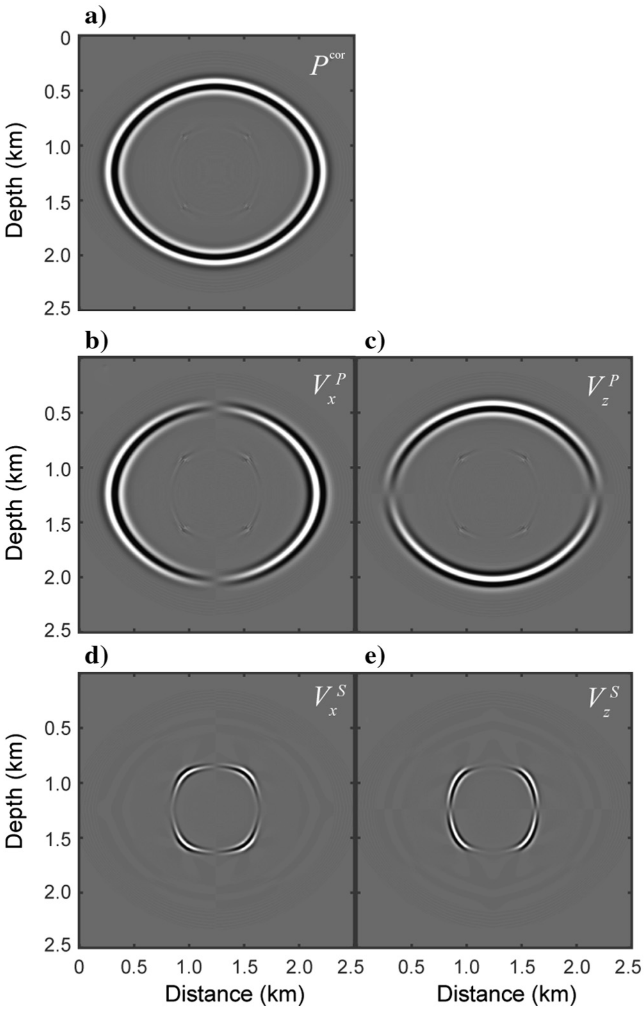

Figure 2. Snapshots of the separated wavefields calculated using equations 12 and 13 in the model used in Figure 1, with (a) scalar qP wave P^{cor}; (b and c) x- and z-components of the separated vector qP wave V_x^P and V_z^P, and (d and e) x- and z-components of the separated vector qSV wave V_x^S and V_z^S.

Table 1. The Thomsen anisotropic parameters for 2D homogeneous VTI models.

Model no.	V_{P0} (m/s)	V_{S0} (m/s)	ρ (kg/m^3)	ε	δ
1	3000	1500	1.8	0.25	–0.29
2	3000	1500	1.8	0.29	0.25
3	3000	1500	1.8	0.1	–0.1
4	3000	1500	1.8	0.1	0.1

where S_k is a wavenumber-domain scalar operator and can be expressed as

$$S_k = \frac{-(c_{11}-c_{44})k_x^2 + (c_{33}-c_{44})k_z^2 + D_k}{2(c_{13}+c_{44})k_z^2}. \tag{3}$$

By defining a local qP-wave unit propagation direction vector $\mathbf{n} = (n_x, n_z) = \mathbf{k}/|\mathbf{k}|$, S_k can be transformed to a space-domain scalar operator:

$$S_n = \frac{-(c_{11}-c_{44})n_x^2 + (c_{33}-c_{44})n_z^2 + D_n}{2(c_{13}+c_{44})n_z^2}, \tag{4}$$

where $D_n = \sqrt{[(c_{11}-c_{44})n_x^2-(c_{33}-c_{44})n_z^2]^2+4(c_{13}+c_{44})^2n_x^2n_z^2}$. Therefore, S_n can be calculated through vector $\mathbf{n}$.

Following Zhou and Wang (2017), $\mathbf{n}$ can be obtained by calculating the wave propagation direction using the Poynting vector, which is a fast and low-cost way to estimate the local propagation direction (Yoon and Marfurt, 2006). Theoretically, the qP wave propagation direction can only be accurately determined after the wavefield separation. Here, we first generate an initial qP wavefield and roughly estimate the propagation direction. This initial qP wavefield does not have to be very accurate. Thus, we apply a divergence calculation to the coupled elastic wavefield to obtain an initial qP wavefield, followed by calculating its Poynting vector and using this as an estimate for the local propagation direction. Because only a normalized propagation direction is required, the time derivative in the Poynting vector can be ignored. This yields an estimation of the unit qP wave propagation vector:

$$\begin{cases} n_x = s_x/|\mathbf{s}| \\ n_z = s_z/|\mathbf{s}| \end{cases}, \tag{5}$$

where $\mathbf{s} = \nabla(\sigma_{xx}+\sigma_{zz})$, and σ_{xx} and σ_{zz} are normal stress wavefields. Therefore, the scalar operator S_n can be obtained fully in the space domain.

Next, we transform the wavenumber-domain separation operator $i\hat{\mathbf{a}}_1$ into the space domain and obtain the separation operator ∇^{VTI} in 2D VTI media:

$$\nabla^{\mathrm{VTI}} = \begin{bmatrix} \frac{\partial}{\partial x} \\ S_n \frac{\partial}{\partial z} \end{bmatrix}. \tag{6}$$

In an isotropic media, i.e., $\varepsilon = \delta = 0$, $S_n = S_k = 1$, equation 6 degenerates to the conventional isotropic separation operator:

$$\nabla = \begin{bmatrix} \frac{\partial}{\partial x} \\ \frac{\partial}{\partial z} \end{bmatrix}. \tag{7}$$

We extend the wavefield separation theory in Fan et al. (2022) for isotropic media to the anisotropic case. For detailed derivation, please refer to Appendix B. Assuming the original coupled velocity wavefield is $\mathbf{V} = (V_x, V_z)$, the Helmholtz potentials of the qP and qSV waves, denoted by P and $\mathbf{S}$, are

$$\begin{cases} P = \nabla^{\mathrm{VTI}} \cdot \mathbf{V} \\ \mathbf{S} = \nabla^{\mathrm{VTI}} \times \mathbf{V} \end{cases}, \tag{8}$$

and the amplitude- and phase-corrected Helmholtz potentials of the qP and qSV waves, denoted by P^{cor} and $\mathbf{S}^{\mathrm{cor}}$, are (Zhang and McMechan, 2010; Fan et al., 2022)

$$\begin{cases} \frac{\partial P^{\mathrm{cor}}}{\partial t} = \alpha_n^{\mathrm{VTI}} P = \alpha_n^{\mathrm{VTI}} \nabla^{\mathrm{VTI}} \cdot \mathbf{V} \\ \frac{\partial \mathbf{S}^{\mathrm{cor}}}{\partial t} = \beta_n^{\mathrm{VTI}} \mathbf{S} = \beta_n^{\mathrm{VTI}} \nabla^{\mathrm{VTI}} \times \mathbf{V} \end{cases}, \tag{9}$$

where α_n^{VTI} and β_n^{VTI} are the space-domain scalar operators and can be expressed as

$$\begin{cases} \alpha_n^{\mathrm{VTI}} = \sqrt{\frac{1}{2\rho}\frac{[(c_{11}+c_{44})n_x^2+(c_{33}+c_{44})n_z^2+D_n]}{n_x^2+S_n^2n_z^2}} \\ \beta_n^{\mathrm{VTI}} = \sqrt{\frac{1}{2\rho}\frac{[(c_{11}+c_{44})n_x^2+(c_{33}+c_{44})n_z^2-D_n]}{n_x^2+S_n^2n_z^2}} \end{cases}, \tag{10}$$

where P^{cor} is also regarded as the scalar qP wave and can be directly used in the following PP image during ERTM. The vector qP and

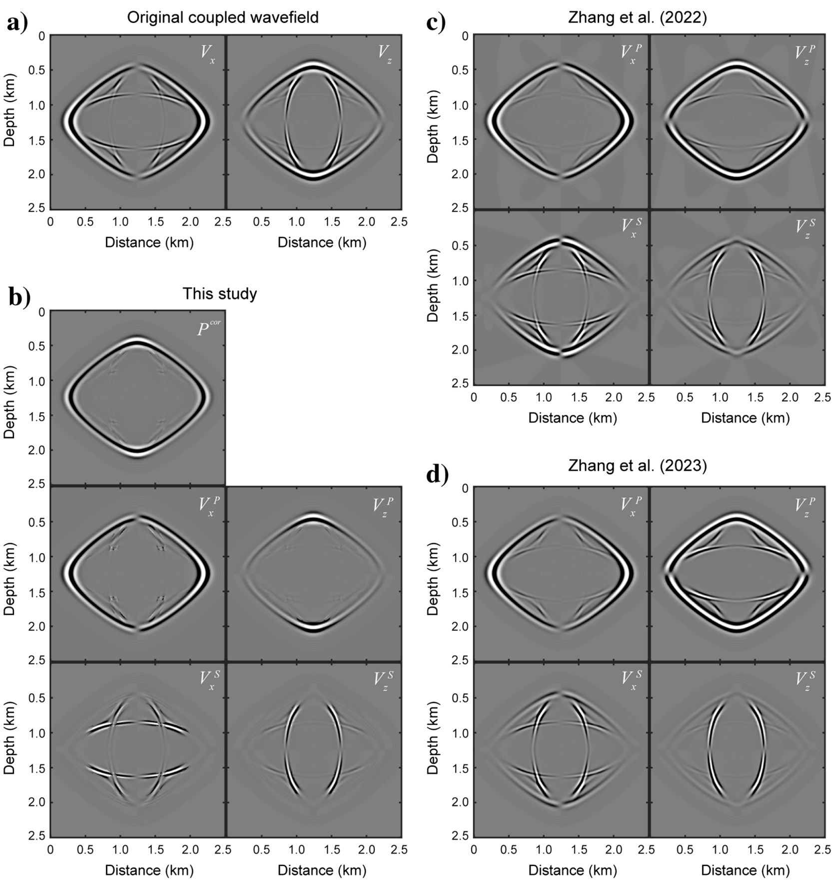

Figure 3. The wavefield separation of model 1 in Table 1. The snapshots are (a) the original coupled wavefield, (b) the separated wavefield using our method, (c) using the method by Zhang et al. (2022), and (d) using the method by Zhang et al. (2023). The names of the methods are indicated on the top of each panel; V_x and V_z are the x- and z-components of the coupled wavefield; P^{cor} is the scalar qP wavefield; V_x^P and V_z^P are the x- and z-components of the separated vector qP wavefield; and V_x^S and V_z^S are the x- and z-components of the separated qSV wave components.

qSV waves, denoted by $\mathbf{V}^P$ and $\mathbf{V}^S$, can be calculated by solving (Zhang and McMechan, 2010; Fan et al., 2022)

$$\begin{cases} \frac{\partial^2 \mathbf{V}^P}{\partial t^2} = \alpha_n^{\mathrm{VTI}} \nabla^{\mathrm{VTI}} P^{\mathrm{cor}} = (\alpha_n^{\mathrm{VTI}})^2 \nabla^{\mathrm{VTI}} \cdot (\nabla^{\mathrm{VTI}} \cdot \mathbf{V}) \\ \frac{\partial^2 \mathbf{V}^S}{\partial t^2} = -\beta_n^{\mathrm{VTI}} \nabla^{\mathrm{VTI}} \times \mathbf{S}^{\mathrm{cor}} = -(\beta_n^{\mathrm{VTI}})^2 \nabla^{\mathrm{VTI}} \times (\nabla^{\mathrm{VTI}} \times \mathbf{V}) \end{cases}. \tag{11}$$

Finite-difference schemes are used to solve equations 8, 9, and 11. However, we find that the wavefields separated using equations 9 and 11 often show some errors, which we demonstrate using numerical examples. A homogeneous VTI model is used for this purpose. The model parameters are $v_{P0} = 3000$ m/s, $v_{S0} = 1500$ m/s, $\varepsilon = 0.2$, and $\delta = 0.1$, and an explosive source is located at the center of the model. Figure 1 gives snapshots of the coupled and separated wavefields, i.e., P^{cor} (Figure 1c), S^{cor} (Figure 1h), V_x^P (Figure 1d), V_z^P (Figure 1e), V_x^S (Figure 1i), and V_z^S (Figure 1j). By checking these separated wavefields, we see certain near-field noise around the source. Similar tests are conducted for different anisotropic parameters, and the results show that the noise is larger for models with stronger anisotropy. This phenomenon occurs because all scalar operators, S_n, α_n^{VTI}, and β_n^{VTI}, are calculated based on the estimations of the propagation directions of the initial qP wavefield, and the embedded errors lead to accumulated errors during the time iterations in equations 9 and 11. Using the Poynting vector to estimate the propagation direction is not highly accurate, especially for complicated wavefields, because it only represents the sum direction of different waves. In an isotropic medium, equations 9 and 11 degenerate to the isotropic case in Fan et al. (2022), wherein no errors are generated. Therefore, directly solving equations 9 and 11 is not an ideal method of separation. An alternative method is used to alleviate this difficulty.

Scalar qP wave

In the subsequent ERTM, we only need the scalar qP wave P^{cor} for the PP image and the vector qP and qSV waves for the PS image. We first calculate the P^{cor}. Because P^{cor} is directly related to the stress, we can take a shortcut to retrieve it. The detailed derivation is given in Appendix B, and the final result is

$$P^{\mathrm{cor}} = \alpha_n^{\mathrm{VTI}} \frac{[(c_{33} - c_{13} S_n)\sigma_{xx} + (S_n c_{11} - c_{13})\sigma_{zz}]}{c_{11}c_{33} - c_{13}^2}. \tag{12}$$

For an isotropic medium, i.e., $\varepsilon = \delta = 0$, it directly degenerates to $P^{\mathrm{cor}} = \sqrt{(\lambda + 2\mu)/(2\rho(\lambda+\mu))}(\sigma_{xx} + \sigma_{zz})$, where λ and μ are Lamé coefficients in an isotropic medium. This is exactly the 2D isotropic result given by Zhou et al. (2019).

Vector wavefield decomposition

To decompose the coupled waves into vector qP and qSV waves, the key issue is dealing with the second-order time derivatives in equation 11. Naturally, it can be transformed into the quadratic integration of the coupled wavefield, which can be denoted by $\mathbf{V}''$ and satisfies $\partial^2 \mathbf{V}''/\partial t^2 = \mathbf{V}$. This equation can be solved during the time iteration but after several numerical tests, we find it has poor stability. Alternatively, following Yang et al. (2018), we first apply the filter $-1/\omega^2$ to the source wavelet as well as multicomponent seismic records and then complete the finite-difference forward modeling to obtain the $\mathbf{V}''$. Finally, the following equations are used to obtain the decomposed vector qP and qSV wavefields:

$$\begin{cases} \mathbf{V}^P = (\alpha_n^{\mathrm{VTI}})^2 \nabla^{\mathrm{VTI}} \cdot (\nabla^{\mathrm{VTI}} \cdot \mathbf{V}'') \\ \mathbf{V}^S = -(\beta_n^{\mathrm{VTI}})^2 \nabla^{\mathrm{VTI}} \times (\nabla^{\mathrm{VTI}} \times \mathbf{V}'') \end{cases}. \tag{13}$$

Figure 2 shows the separated wavefield snapshots calculated using equations 12 and 13 in the same VTI model as used in Figure 1. By comparing Figures 1 and 2, we see that all snapshots P^{cor} (Figure 2a), V_x^P and V_z^P (Figure 2b and 2c), and V_x^S and V_z^S (Figure 2d and 2e) show much higher accuracy compared with those obtained by directly solving equations 9 and 11.

Anisotropic ERTM

For anisotropic ERTM, a dot-product imaging condition based on the decomposed vector wavefield is often used (e.g., Yang et al.,

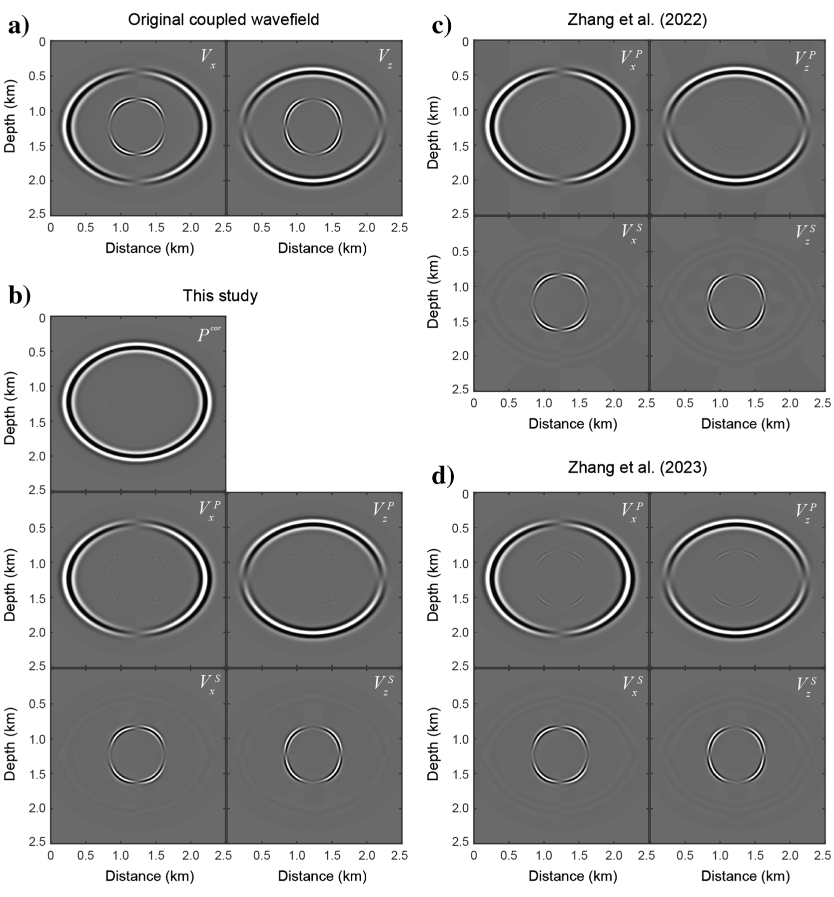

Figure 4. (a–d) Similar to Figure 3a–3d, except it is for model 2 in Table 1.

2019; Zhang et al., 2022, 2023; Zuo et al., 2022). However, this form of imaging condition, even for isotropic media, involves an additional factor, which is the cosine or sine function of the angle between the incident and reflection directions, leading to errors in estimating the reflection coefficients (Zhang and Shi, 2019; Zhou et al., 2019). Alternatively, for anisotropic media, we use a scalar imaging condition for the PP image and a magnitude- and sign-based vector imaging condition for the PS image (Fan et al., 2022):

$$I^{\mathrm{PP}}(\mathbf{x}) = \frac{\int_0^{T_{\max}} P_{\mathrm{src}}^{\mathrm{cor}}(\mathbf{x},t)P_{\mathrm{rec}}^{\mathrm{cor}}(\mathbf{x},t)dt}{\int_0^{T_{\max}} P_{\mathrm{src}}^{\mathrm{cor}}(\mathbf{x},t)^2 dt}, \tag{14a}$$

$$I^{\mathrm{PS}}(\mathbf{x}) = \frac{\int_0^{T_{\max}} \mathrm{sgn}^{PS}(\mathbf{x},t)|\mathbf{V}_{\mathrm{src}}^{P}(\mathbf{x},t)||\mathbf{V}_{\mathrm{rec}}^{S}(\mathbf{x},t)|dt}{\int_0^{T_{\max}} |\mathbf{V}_{\mathrm{src}}^{P}(\mathbf{x},t)|^2 dt}, \tag{14b}$$

where I^{PP} and I^{PS} are the PP and PS images, the subscripts src and rec denote the source- and receiver-side wavefields, and the operator $|\cdot|$ denotes taking the amplitude of a vector. The $\mathrm{sgn}^{\mathrm{PP}}$ and $\mathrm{sgn}^{\mathrm{PS}}$ are

$$\mathrm{sgn}^{\mathrm{PP}}(\mathbf{x},t) = \begin{cases} +1, \mathbf{V}_{\mathrm{src}}^{P}(\mathbf{x},t)\cdot\mathbf{V}_{\mathrm{rec}}^{P}(\mathbf{x},t) > 0 \\ -1, \mathbf{V}_{\mathrm{src}}^{P}(\mathbf{x},t)\cdot\mathbf{V}_{\mathrm{rec}}^{P}(\mathbf{x},t) < 0 \end{cases}, \tag{15a}$$

$$\mathrm{sgn}^{\mathrm{PS}}(\mathbf{x},t) = \begin{cases} +1, \mathbf{V}_{\mathrm{src}}^{P}(\mathbf{x},t)\cdot\mathbf{V}_{\mathrm{rec}}^{S}(\mathbf{x},t) > 0 \\ -1, \mathbf{V}_{\mathrm{src}}^{P}(\mathbf{x},t)\cdot\mathbf{V}_{\mathrm{rec}}^{S}(\mathbf{x},t) < 0 \end{cases}, \tag{15b}$$

where the operator "·" denotes the dot product between two vectors.

Following the preceding discussion for anisotropic ERTM, the procedures to generate the PP and PS images are slightly different and summarized next. The workflow for the PP image is as follows:

1) Extrapolate the source wavefield using the elastic VTI finite-difference propagator. Use equation 12 to obtain the source-side scalar qP wavefield $P_{\mathrm{src}}^{\mathrm{cor}}$.
2) Extrapolate the receiver-side adjoint wavefield using the elastic VTI finite-difference propagator. Similarly, use equation 12 to obtain the receiver-side scalar qP wavefields $P_{\mathrm{rec}}^{\mathrm{cor}}$.
3) Apply the scalar imaging condition, equation 14a, to generate PP-reflectivity images.

The workflow for the PS image is as follows.

1) Integrate the source wavelet and multicomponent seismic records twice over time or, equivalently, filter them with $-1/\omega^2$.
2) Calculate the source wavefield using the integrated source time function and the elastic VTI propagator. Use equation 13 to obtain the source-side vector qP wavefield $\mathbf{V}_{\mathrm{src}}^{P}$.
3) Use the elastic VTI propagator to extrapolate the integrated multicomponent records to obtain the adjoint wavefield. Use equation 13 to obtain the receiver-side vector qSV wavefield $\mathbf{V}_{\mathrm{rec}}^{S}$.
4) Apply the magnitude- and sign-based vector imaging condition, equation 14b, to generate the PS-reflectivity image.

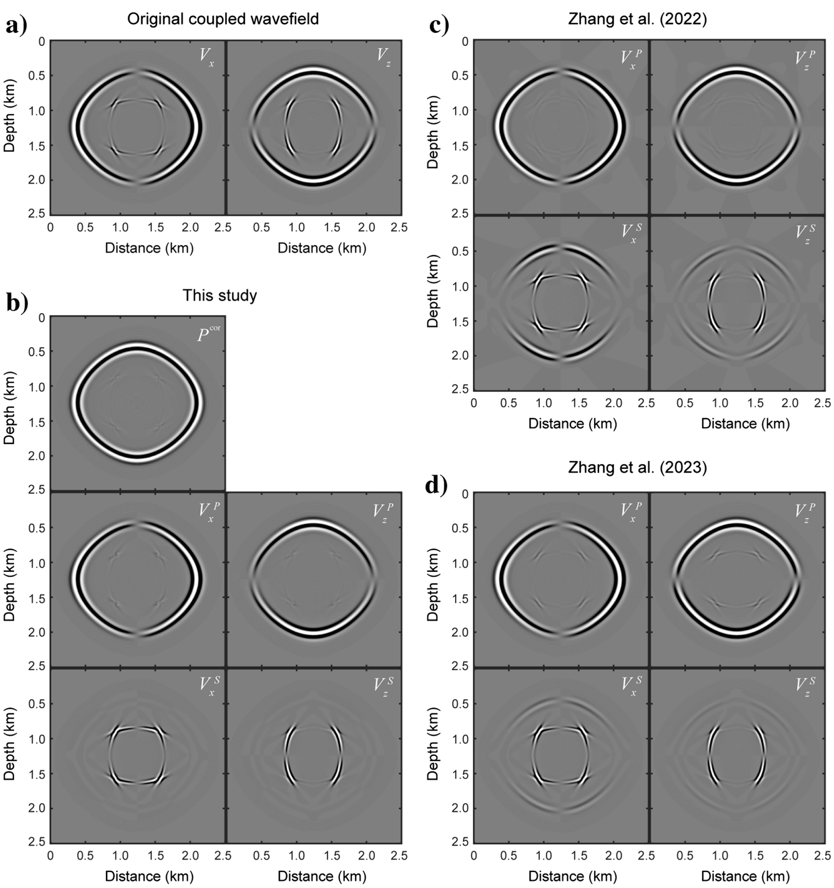

Figure 5. (a–d) Similar to Figure 3a–3d, except it is for model 3 in Table 1.

NUMERICAL EXAMPLES

In this section, we validate the proposed wavefield decomposition scheme and ERTM workflow using the numerical examples in 2D elastic VTI models.

2D homogeneous models

First, we use a group of homogeneous VTI models with different anisotropic parameters to examine the proposed separation method. The results are also compared with those of Zhang et al. (2022, 2023). The four VTI models shown in Table 1 have different ε and δ. Model 4 has elliptical anisotropy, model 2 is close to elliptical anisotropy, and models 1 and 3 have strong anisotropy. Shown in Figures 3–6 are wavefields in these four models. Figures 3a, 4a, 5a, and 6a show the coupled wavefield; Figures 3b, 4b, 5b, and 6b show the wavefields separated using our method; and Figures 3c, 4c, 5c, and 6c and Figures 3d, 4d, 5d, and 6d are wavefields separated using methods proposed by Zhang et al. (2022) and Zhang et al. (2023), respectively.

In Figures 3–6, we see that the methods by Zhang et al. (2022) and Zhang et al. (2023) only achieved high separation accuracy in models 2 and 4 but not in models 1 and 3, wherein their results show severe residual waves. The results demonstrate that the methods by Zhang et al. (2022) and Zhang et al. (2023) only work well in elliptical or near-elliptical anisotropy. However, the proposed method can obtain reasonably accurate results in all four models. By carefully investigating Figures 3–6, the results show that stronger anisotropy tends to reduce the separation accuracy. As can be seen in Figure 3b for model 1, the snapshot of V_x^P is still slightly contaminated by residual qSV waves but nevertheless remains much better than the other methods. During the calculation of scalar operators, the local qP-wave unit propagation direction is computed using the Poynting vector of the initial qP wavefield. As discussed previously, the Poynting vector method can sometimes produce poor estimates of the propagation directions. In addition, the initial qP wavefield, obtained by applying a divergence operator to the coupled elastic wavefield, is not a pure qP wavefield. Therefore, minor errors may be introduced during the calculation.

The reason why methods by Zhang et al. (2022) and Zhang et al. (2023) achieve better results for elliptical or near-elliptical models is a result of the fact that they used the operator

$$\nabla^{\mathrm{VTI}} = \left[\begin{array}{c} \frac{\partial}{\partial x} \\ \frac{\sqrt{[(1+2\delta)V_{P0}^2-V_{S0}^2](V_{P0}^2-V_{S0}^2)}}{[(1+2\epsilon)V_{P0}^2-V_{S0}^2]}\frac{\partial}{\partial z} \end{array} \right]. \qquad (16)$$

This separation operator is based on the eigenvectors for the Christoffel equation under the assumption of elliptical anisotropy (Yang et al., 2019), which has larger errors when the model is biased from the elliptical anisotropy. In contrast, our separation is based on the exact eigenvectors but calculated according to the roughly estimated propagation vector, which slightly affects the decomposition accuracy. Numerical tests validate this.

2D layered model

In the second example, we verify the wavefield separation method and ERTM using a three-layer VTI model. The model size is 3200 m × 1200 m, and the anisotropic parameters are given in Figure 7a. An explosive source with a 25 Hz Ricker wavelet is injected at (1600 m and 40 m). The model is gridded with a spacing interval of 4 m, and the time interval is 0.4 ms. The separated wavefields using the proposed method are shown in Figure 7b–7h, in which Figure 7b and 7c shows the original coupled wavefields. Figure 7d is the scalar qP wavefield. Figure 7e and 7f are the decomposed vector qP wavefields. Figure 7g and 7h are the decomposed vector qSV wavefields. All separated wavefields show good accuracy and can be used in the following ERTM. Figure 8 shows the ERTM results from a one-shot acquisition system, wherein Figure 8a is the PP image from the scalar imaging condition (equation 14a), and Figure 8b is the PS image from the amplitude- and sign-based imaging condition (equation 14b). Figure 8c and 8d are PP and PS images using the dot-product imaging condition. We see in Figure 8c that the polarity of PP reflectivity is reversed (indicated by the black arrows) at very wide incident angles. In Figure 8d, the PS reflectivity is weakened near the normal incidence (indicated by the black arrows) compared with Figure 8b. Therefore, the PP image using the scalar imaging condition and the PS image using the amplitude- and sign-based imaging conditions can better preserve real reflectivities.

A more realistic 2D VTI model

As the last example, we investigate the capability of our wavefield separation method and its applications in ERTM in the modified Marmousi2 velocity model (Martin et al., 2002). Anisotropic parameters V_{P0}, ρ, ε, and δ are given in Figure 9, and the V_{S0} is derived from V_{P0} according to $V_{S0} = V_{P0}/\sqrt{3}$. The migration velocity model is obtained by smoothing the original model using a 40 m × 40 m Gaussian box filter. The model grid size is 561 × 1001 with a spacing interval of 4 m. The time interval is 0.4 ms. In total, 99 explosive sources with a 25 Hz Ricker wavelet are evenly located on the surface with a shot spacing of 40 m.

We first use a source at a distance x = 2 km to examine the performance of our wavefield separation method. Figure 10b and 10c shows the x- and z-components of the coupled elastic wavefield in the migration model. Figure 10d shows the scalar qP wavefield. Figure 10e and 10f shows the x- and z-components of the qP-wave,

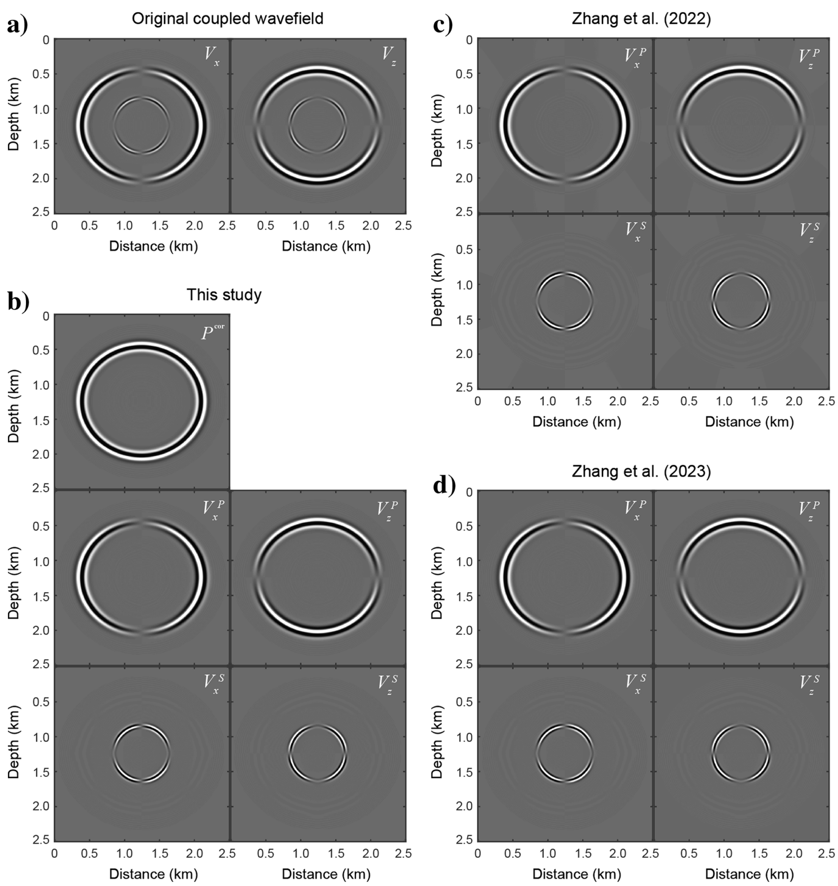

Figure 6. (a–d) Similar to Figure 3a–3d, except it is for model 4 in Table 1.

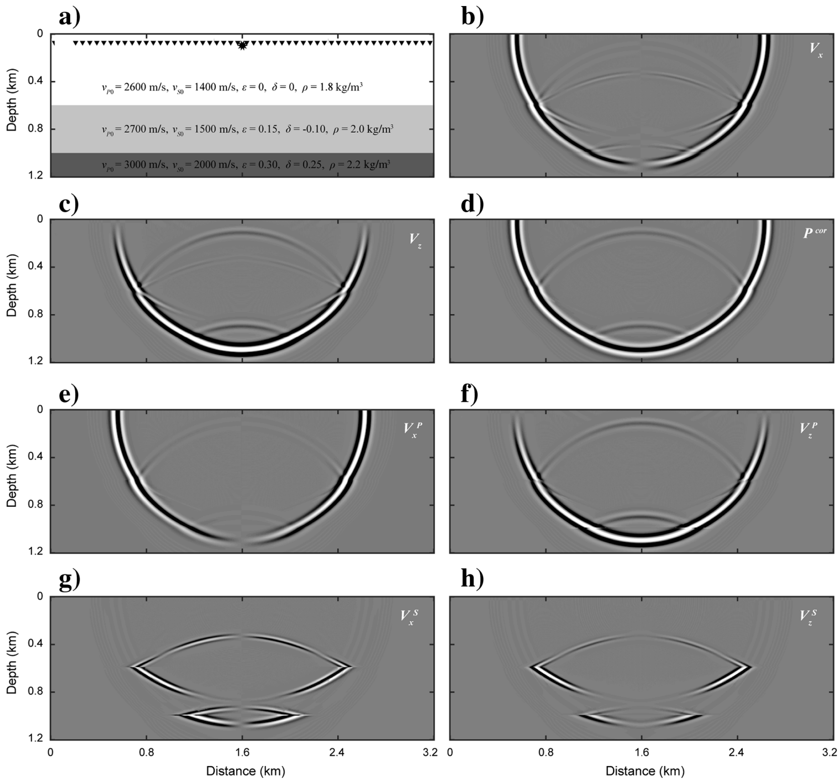

Figure 7. The three-layer VTI model and related wavefield separations. (a) Model geometry, layer parameters, and distributions of the source (star) and receivers (inverse triangles). The snapshots are (b) the x-component V_x and (c) the z-component V_z of the original coupled wavefield, (d) the scalar qP wavefield (P^{cor}), (e) the x-component V_x^P and (f) the z-component V_z^P of the decomposed vector qP wavefield, (g) the x-component V_x^S and (h) the z-component V_z^S of the decomposed vector qSV wavefield. The wave types and components are labeled in individual panels.

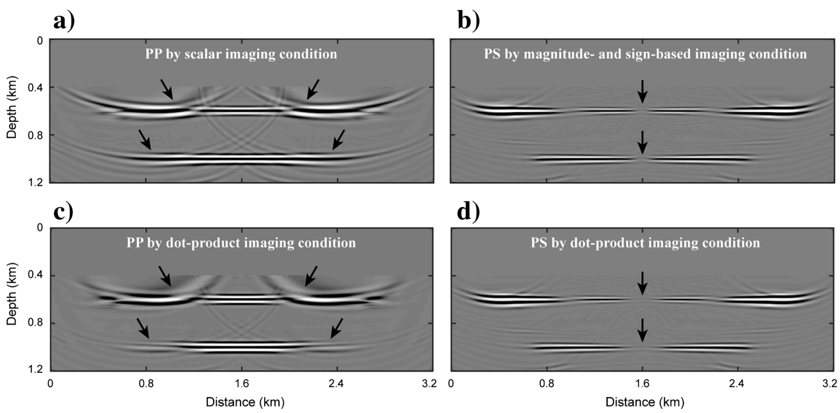

Figure 8. The ERTM image results for a one-shot acquisition system in the three-layer VTI model. (a) PP image using the scalar imaging condition (equation 14a), (b) PS image using the amplitude- and sign-based imaging condition (equation 14b), (c) PP image using the dot-product imaging condition, and (d) PS image using the dot-product imaging condition.

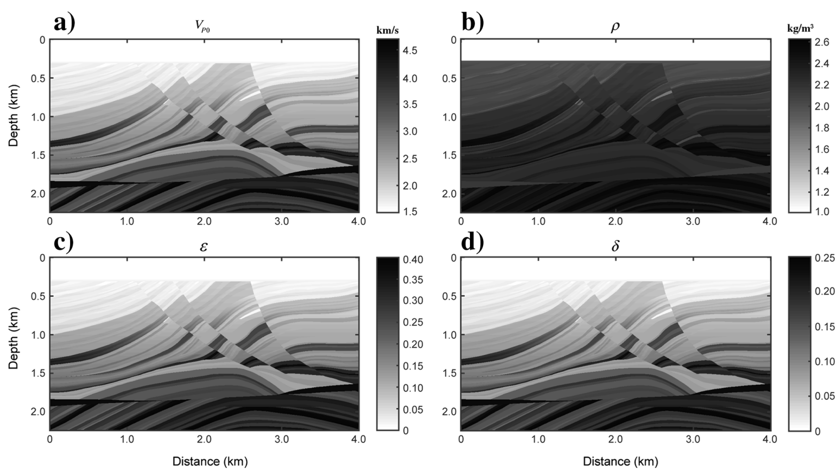

Figure 9. The VTI model modified from the Marmousi2 velocity model. (a–d) The distribution of V_{P0}, ρ, ε, and δ.

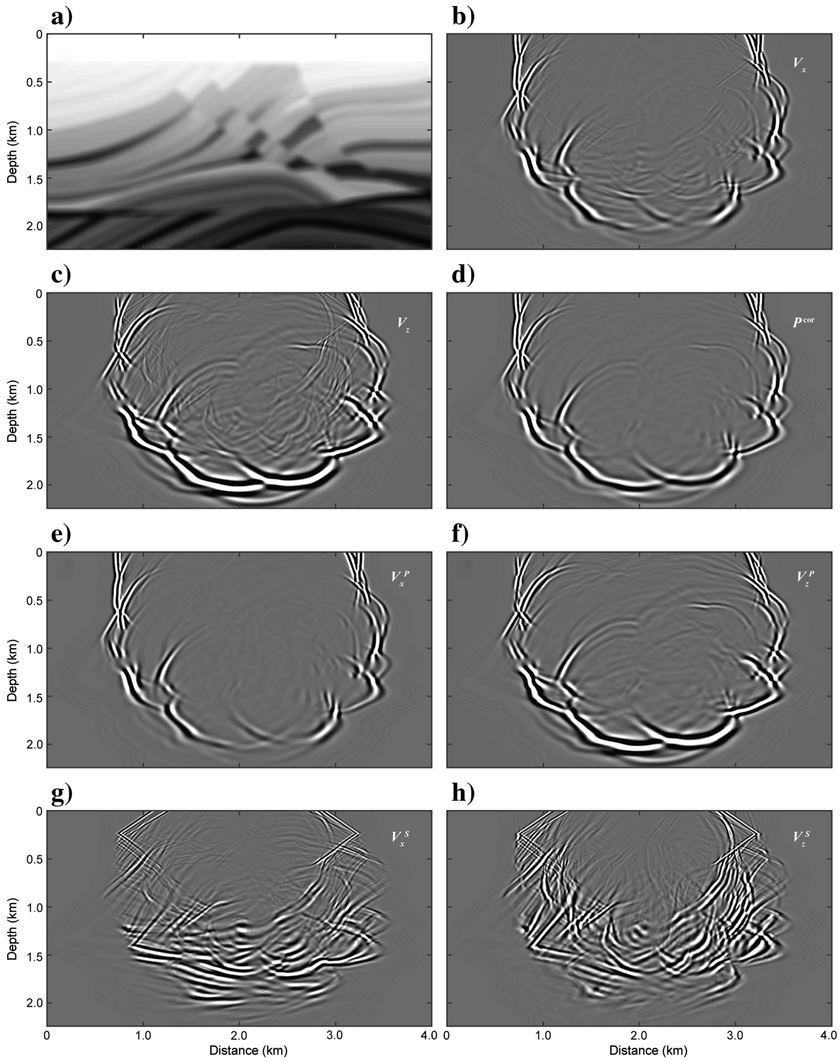

Figure 10. Wavefield separation results using our method. (a) The migration velocity model V_{P0}; (b and c) the x- and z-components of the coupled elastic wavefield, (d) the scalar qP wavefield; (e and f) the x- and z-components of the qP wave, and (g and h) the x- and z-components of the qSV wave. The wave types and components are indicated in the figure.

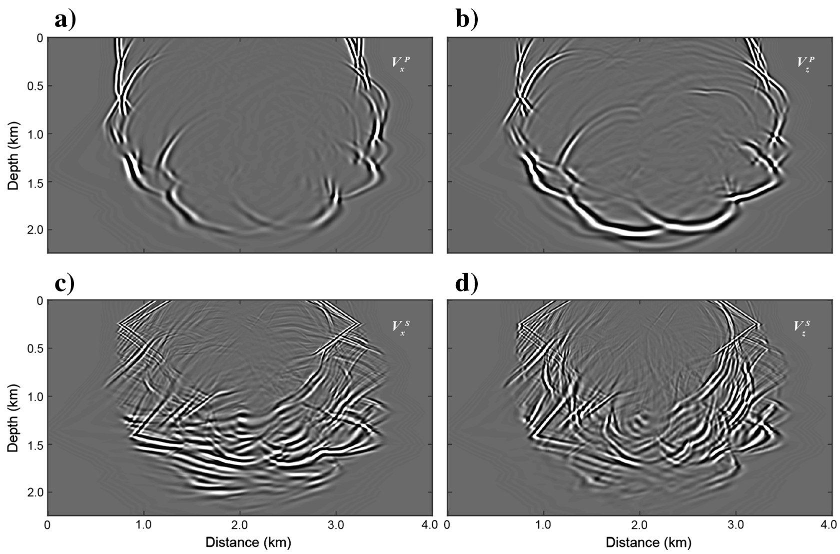

Figure 11. Wavefield separation results using Zhang et al. (2023)'s method. (a and b) The x- and z-components of the qP wave, and (c and d) the x- and z-components of the qSV wave. The wave types and components are indicated in the figure.

respectively. Figure 10g and 10h shows the x- and z-components of the qSV wave. As expected, these results again present a satisfactory separation accuracy. Figure 11 shows the wavefield separation results using Zhang et al.'s (2023) method. For this model, δ is slightly smaller than ε almost everywhere, which can be regarded as a near-elliptical VTI medium. Therefore, the separation results of both show good accuracy. Figure 12 shows the PP and PS images using the aforementioned ERTM method and Zhang et al.'s (2023) ERTM method. Zhang et al. (2023) obtain the decomposed vector qP and qS wavefields and use the dot-product vector imaging condition to produce the PP and PS images. We extract two traces at distances of 1.84 and 2.8 km in PP and PS images and compare them in Figure 13. Due to the multishot stacking effect and narrow aperture, the images from the dot-product vector imaging conditions are very close to those from the scalar and magnitude- and sign-based vector imaging conditions, especially for the PS image, but have slightly smaller amplitudes due to the cosine/sine factors involved (Zhou et al., 2019; Fan et al., 2022). PP images using the dot-product vector imaging condition still have some amplitude and phase differences compared with the images from the scalar imaging conditions, especially at shallow depths because the superwide opening angles at large offset cause polarity reversal. Therefore, the PP from the scalar imaging conditions and the PS from the magnitude- and sign-based vector imaging conditions can provide high-fidelity elastic true reflectivity images.

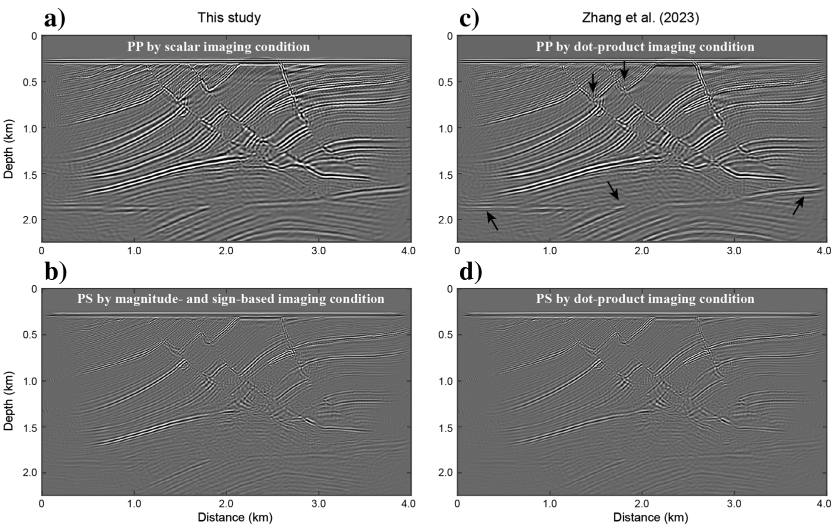

Figure 12. Comparison between the anisotropic ERTM results using our method and the method of Zhang et al. (2023) for the modified Marmousi2 velocity model shown in Figure 9. (a) The PP image using our method with the scalar imaging condition (equation 14a), (b) the PS image with the amplitude- and sign-based imaging condition (equation 14b), and (c and d) the PP and PS images using the dot-product imaging condition in Zhang et al. (2023).

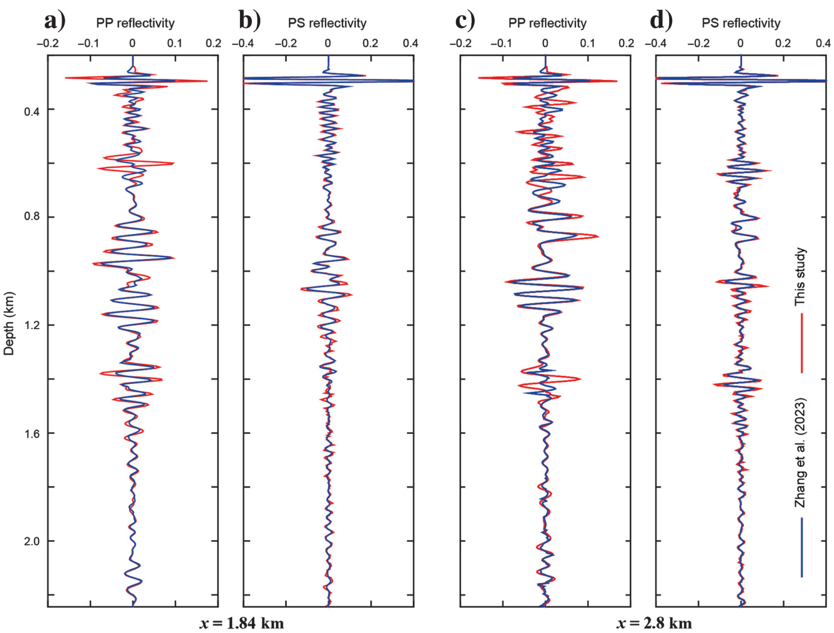

Figure 13. Comparisons among the different image traces in the Marmousi2 model (a and b) at a horizontal distance of 1.84 km and (c and d) at 2.8 km, for (a and c) the PP image and (b and d) the PS image. The blue lines are images using the dot-product vector imaging condition, and the red lines are using the magnitude- and sign-based vector imaging condition.

CONCLUSION

A wavefield separation operator for the VTI models is constructed using the qP wave polarization directions, which are also eigenvectors of the Christoffel equation. The original separation operator is defined in the mixed space-wavenumber domain. We introduce scalar operators to transform the space-wavenumber operation into a space-domain operation. The local wave propagation direction in the space domain is estimated using the Poynting vector. Thus, the resulting wavefield separation can be efficiently calculated in the space domain with a graphics processing unit. To perform ERTM using the separated P and S waves, we not only obtain the decomposed vector qP and qSV wavefields but also retrieve the scalar qP wavefield. These separated scalar and vector wavefields have the same amplitude and phase information as the original coupled wavefield. For anisotropic ERTM, we propose to use the scalar imaging condition to generate the PP image and the magnitude- and sign-based vector imaging condition to produce the PS image; both have higher image accuracy than the conventional dot-product image condition. Finally, we use 2D numerical examples to validate the proposed wavefield separation method in the VTI models and their applications in ERTM for the PP- and PS-reflectivity images.

ACKNOWLEDGMENTS

The authors thank the editors and four reviewers for their critical comments that greatly improved this manuscript. This work was financially supported by the National Natural Science Foundation of China (grant nos. 41604037 and 41974061) and the Hubei Provincial Natural Science Foundation of China (grant no. 2022CFB125).

DATA AND MATERIALS AVAILABILITY

Data associated with this research are available and can be obtained by contacting the corresponding author.

APPENDIX A

THE POLARIZATION DIRECTIONS OF QP AND QSV WAVES

Following Tsvankin (2012), substituting a plane wave into the anisotropic elastic wave equation leads to the so-called Christoffel equation for the phase velocity V and polarization vector $\mathbf{U}$:

$$[\mathbf{\Gamma} - \rho V^2 \mathbf{I}]\mathbf{U} = 0, \tag{A-1}$$

where $\mathbf{\Gamma}$ is the Christoffel matrix related to the stiffness matrix c_{ij} and the propagation direction $\mathbf{n} = (\sin\theta, \cos\theta)^{\mathrm{T}}$. The preceding equation forms a standard 3×3 eigenvalue problem. For a positive symmetric matrix $\mathbf{\Gamma}$, eigenvalues can be obtained by solving

$$\det|\mathbf{\Gamma} - \rho V^2 \mathbf{I}| = 0. \tag{A-2}$$

In a 2D VTI case, the Christoffel matrix degenerates to a 2×2 matrix, which can be expressed as

$$\mathbf{\Gamma} = \begin{bmatrix} c_{11}\sin^2\theta + c_{44}\cos^2\theta & (c_{13}+c_{44})\sin\theta\cos\theta \\ (c_{13}+c_{44})\sin\theta\cos\theta & c_{44}\sin^2\theta + c_{33}\cos^2\theta \end{bmatrix}. \tag{A-3}$$

Solving equation A-2 gives eigenvalues

$$\rho V^2 = \frac{1}{2}[(c_{11}+c_{44})\sin^2\theta + (c_{33}+c_{44})\cos^2\theta \pm D_\theta]. \tag{A-4}$$

Substituting them back to equation A-1, we have the corresponding eigenvectors

$$\mathbf{U} = \begin{bmatrix} 2(c_{13}+c_{44})\sin\theta\cos\theta \\ -(c_{11}-c_{44})\sin^2\theta + (c_{33}-c_{44})\cos^2\theta \pm D_\theta \end{bmatrix}, \tag{A-5}$$

where $D_\theta = \sqrt{[(c_{11}-c_{44})\sin^2\theta - (c_{33}-c_{44})\cos^2\theta]^2 + 4(c_{13}+c_{44})^2 \sin^2\theta\cos^2\theta}$.

The two eigenvalues and the corresponding eigenvectors relate to the phase velocities and polarization directions of two propagation modes, with "+" denoting the qP wave and "–" denoting the qS wave, respectively. Using relations $\sin\theta = k_x/k$ and $\cos\theta = k_z/k$, where k is the wavenumber, the two eigenvectors in equation A-5 can be further expressed as

$$\hat{\mathbf{a}}_1 = \begin{bmatrix} k_x \\ \frac{-(c_{11}-c_{44})k_x^2 + (c_{33}-c_{44})k_z^2 + D_k}{2(c_{13}+c_{44})k_z^2} k_z \end{bmatrix}, \tag{A-6a}$$

$$\hat{\mathbf{a}}_2 = \begin{bmatrix} k_x \\ \frac{-(c_{11}-c_{44})k_x^2 + (c_{33}-c_{44})k_z^2 - D_k}{2(c_{13}+c_{44})k_z^2} k_z \end{bmatrix}, \tag{A-6b}$$

to give the wavenumber domain polarization directions of the qP and qS waves, where $D_k = \sqrt{[(c_{11}-c_{44})k_x^2 - (c_{33}-c_{44})k_z^2]^2 + 4(c_{13}+c_{44})^2 k_x^2 k_z^2}$.

APPENDIX B

WAVEFIELD SEPARATION EQUATIONS IN 2D VTI MEDIA

We derive the wavefield separation equations following Fan et al. (2022) for the isotropic case. In an anisotropic medium, the Helmholtz potentials for the P and S waves are

$$\begin{cases} P = \nabla^{\mathrm{VTI}} \cdot \mathbf{V} \\ \mathbf{S} = \nabla^{\mathrm{VTI}} \times \mathbf{V} \end{cases}, \tag{B-1}$$

where ∇^{VTI} is the anisotropic separation operator in equation 6. We use P^{cor} and $\mathbf{S}^{\mathrm{cor}}$ to denote the amplitude- and phase-corrected Helmholtz potential of the qP and qSV waves, which can be expressed in the wavenumber domain as (Zhang and McMechan, 2010; Fan et al., 2022)

$$\begin{cases} \hat{P}^{\mathrm{cor}} = \mathbf{I}^{\mathrm{VTI}} \cdot \hat{\mathbf{V}} \\ \hat{\mathbf{S}}^{\mathrm{cor}} = \mathbf{I}^{\mathrm{VTI}} \times \hat{\mathbf{V}} \end{cases}, \tag{B-2}$$

where $\mathbf{I}^{\mathrm{VTI}} = \left(1/\sqrt{k_x^2 + S_k^2 k_z^2}\right)\begin{bmatrix} k_x \\ S_k k_z \end{bmatrix}$ is the normalized vector of the qP-wave polarization vector $\hat{\mathbf{a}}_1$ in equation 1a. We rewrite equation B-2 into

$$\begin{cases} \hat{P}^{\mathrm{cor}} = \frac{1}{ik}\sqrt{\frac{k_x^2+k_z^2}{k_x^2+S_k^2k_z^2}} i\hat{\mathbf{a}}_1 \cdot \hat{\mathbf{V}} \\ \hat{\mathbf{S}}^{\mathrm{cor}} = \frac{1}{ik}\sqrt{\frac{k_x^2+k_z^2}{k_x^2+S_k^2k_z^2}} i\hat{\mathbf{a}}_1 \times \hat{\mathbf{V}} \end{cases}. \tag{B-3}$$

In addition, we have the dispersion relations $k = \omega/V_P(\theta)$ for the qP wave and $k = \omega/V_S(\theta)$ for the qSV wave in a VTI medium. Here, $V_P(\theta)$ and $V_S(\theta)$ are the phase velocities of the qP and qSV waves, respectively. According to equation A-4, they are related to the propagation direction θ and can be expressed by (Tsvankin, 2012)

$$\begin{cases} V_P(\theta) = \sqrt{\frac{1}{2\rho}[(c_{11}+c_{44})\sin^2\theta + (c_{33}+c_{44})\cos^2\theta + D_\theta]} \\ V_S(\theta) = \sqrt{\frac{1}{2\rho}[(c_{11}+c_{44})\sin^2\theta + (c_{33}+c_{44})\cos^2\theta - D_\theta]} \end{cases}. \tag{B-4}$$

Substituting these dispersion relations for the wavenumbers in equation B-3, we have

$$\begin{cases} \hat{P}^{\mathrm{cor}} = \frac{V_P(\theta)}{i\omega}\sqrt{\frac{k_x^2+k_z^2}{k_x^2+S_k^2k_z^2}}i\hat{\mathbf{a}}_1 \cdot \hat{\mathbf{V}} \\ \hat{\mathbf{S}}^{\mathrm{cor}} = \frac{V_S(\theta)}{i\omega}\sqrt{\frac{k_x^2+k_z^2}{k_x^2+S_k^2k_z^2}}i\hat{\mathbf{a}}_1 \times \hat{\mathbf{V}} \end{cases}. \tag{B-5}$$

Substituting equation B-4 into equation B-5, replacing the wavenumber with the unit propagation direction (similar to substituting S_k with S_n in equation 4), and following by transforming them into the space domain, we finally obtain the space domain equations

$$\begin{cases} \frac{\partial P^{\mathrm{cor}}}{\partial t} = \alpha_n^{\mathrm{VTI}} P = \alpha_n^{\mathrm{VTI}} \nabla^{\mathrm{VTI}} \cdot \mathbf{V} \\ \frac{\partial \mathbf{S}^{\mathrm{cor}}}{\partial t} = \beta_n^{\mathrm{VTI}} \mathbf{S} = \beta_n^{\mathrm{VTI}} \nabla^{\mathrm{VTI}} \times \mathbf{V} \end{cases}, \tag{B-6}$$

where α_n^{VTI} and β_n^{VTI} are both space domain scalar operators and can be expressed by

$$\begin{cases} \alpha_n^{\mathrm{VTI}} = \sqrt{\frac{1}{2\rho}\frac{[(c_{11}+c_{44})n_x^2+(c_{33}+c_{44})n_z^2+D_n]}{n_x^2+S_n^2n_z^2}} \\ \beta_n^{\mathrm{VTI}} = \sqrt{\frac{1}{2\rho}\frac{[(c_{11}+c_{44})n_x^2+(c_{33}+c_{44})n_z^2-D_n]}{n_x^2+S_n^2n_z^2}} \end{cases}, \tag{B-7}$$

where S_n and D_n are introduced in equation 4.

The P^{cor} is also regarded as the scalar qP wave and can be directly used in ERTM for the PP image. The vector qP and qSV waves, denoted by $\mathbf{V}^P$ and $\mathbf{V}^S$, are calculated by (Zhang and McMechan, 2010; Fan et al., 2022)

$$\begin{cases} \hat{\mathbf{V}}^P = \mathbf{I}^{\mathrm{VTI}}(\mathbf{I}^{\mathrm{VTI}} \cdot \hat{\mathbf{V}}) \\ \hat{\mathbf{V}}^S = -\mathbf{I}^{\mathrm{VTI}} \times (\mathbf{I}^{\mathrm{VTI}} \times \hat{\mathbf{V}}) \end{cases}. \tag{B-8}$$

Similarly, following the derivations from equations B-2 to B-6, we can obtain

$$\begin{cases} \frac{\partial^2 \mathbf{V}^P}{\partial t^2} = \alpha_n^{\mathrm{VTI}} \nabla^{\mathrm{VTI}} P^{\mathrm{cor}} = (\alpha_n^{VTI})^2 \nabla^{\mathrm{VTI}} \cdot (\nabla^{\mathrm{VTI}} \cdot \mathbf{V}) \\ \frac{\partial^2 \mathbf{V}^S}{\partial t^2} = -\beta_n^{\mathrm{VTI}} \nabla^{\mathrm{VTI}} \times \mathbf{S}^{\mathrm{cor}} = -(\beta_n^{VTI})^2 \nabla^{\mathrm{VTI}} \times (\nabla^{\mathrm{VTI}} \times \mathbf{V}) \end{cases}. \tag{B-9}$$

Equation B-9 can be regarded as the decoupled elastic-wave equation in 2D VTI media.

APPENDIX C

DERIVATION OF THE SCALAR QP WAVE IN 2D VTI MEDIA

According to the constitutive equations of 2D VTI media, the stress and particle velocity have the following relationship:

$$\begin{cases} \frac{\partial \sigma_{xx}}{\partial t} = c_{11}\frac{\partial v_x}{\partial x} + c_{13}\frac{\partial v_z}{\partial z} \\ \frac{\partial \sigma_{zz}}{\partial t} = c_{13}\frac{\partial v_x}{\partial x} + c_{33}\frac{\partial v_z}{\partial z} \end{cases}, \tag{C-1}$$

where $\mathbf{V} = (v_x, v_z)$ is the velocity wavefield. Equation C-1 can be further rewritten as

$$\begin{cases} \frac{\partial v_x}{\partial x} = \frac{1}{c_{11}c_{33}-c_{13}^2}\left(c_{33}\frac{\partial \sigma_{xx}}{\partial t} - c_{13}\frac{\partial \sigma_{zz}}{\partial t}\right) \\ \frac{\partial v_z}{\partial z} = \frac{1}{c_{11}c_{33}-c_{13}^2}\left(-c_{13}\frac{\partial \sigma_{xx}}{\partial t} + c_{11}\frac{\partial \sigma_{zz}}{\partial t}\right) \end{cases}. \tag{C-2}$$

Substituting it into equation 9 can obtain

$$P^{\mathrm{cor}} = \alpha_n^{\mathrm{VTI}}\frac{[(c_{33} - c_{13}S_n)\sigma_{xx} + (S_nc_{11} - c_{13})\sigma_{zz}]}{c_{11}c_{33} - c_{13}^2}. \tag{C-3}$$

The necessary and sufficient condition for the stable existence of the medium is that its elastic coefficient matrix must be positive definite. It requires $c_{11}c_{33} - c_{13}^2 > 0$ for a 2D VTI medium. In a practical medium, c_{13} is often smaller than c_{11} and c_{33}. Therefore, a zero denominator does not occur.

REFERENCES

Alkhalifah, T., 1998, Acoustic approximations for processing in transversely isotropic media: Geophysics, **63**, 623–631, doi: 10.1190/1.1444361.

Baysal, E., D. D. Kosloff, and J. W. Sherwood, 1983, Reverse time migration: Geophysics, **48**, 1514–1524, doi: 10.1190/1.1441434.

Chang, W.-F., and G. A. McMechan, 1987, Elastic reverse-time migration: Geophysics, **52**, 1365–1375, doi: 10.1190/1.1442249.

Cheng, J., T. Alkhalifah, Z. Wu, P. Zou, and C. Wang, 2016, Simulating propagation of decoupled elastic waves using low-rank approximate mixed-domain integral operators for anisotropic media: Geophysics, **81**, no. 2, T63–T77, doi: 10.1190/geo2015-0184.1.

Cheng, J., and S. Fomel, 2014, Fast algorithms for elastic-wave-mode separation and vector decomposition using low-rank approximation for anisotropic media: Geophysics, **79**, no. 4, C97–C110, doi: 10.1190/geo2014-0032.1.

Dellinger, J., and J. Etgen, 1990, Wave-field separation in two-dimensional anisotropic media: Geophysics, **55**, 914–919, doi: 10.1190/1.1442906.

Du, Q., X. Gong, M. Zhang, Y. Zhu, and G. Fang, 2014, 3D PS-wave imaging with elastic reverse-time migration: Geophysics, **79**, no. 5, S173–S184, doi: 10.1190/geo2013-0253.1.

Du, Q., C. Guo, Q. Zhao, X. Gong, C. Wang, and X.-Y. Li, 2017, Vector-based elastic reverse time migration based on scalar imaging condition: Geophysics, **82**, no. 2, S111–S127, doi: 10.1190/geo2016-0146.1.

Du, Q., Y. Zhu, and J. Ba, 2012, Polarity reversal correction for elastic reverse time migration: Geophysics, **77**, no. 2, S31–S41, doi: 10.1190/geo2011-0348.1.

Duan, Y., and P. Sava, 2015, Scalar imaging condition for elastic reverse time migration: Geophysics, **80**, no. 4, S127–S136, doi: 10.1190/geo2014-0453.1.

Fan, N., X.-B. Xie, L.-F. Zhao, X. Zhou, and Z.-X. Yao, 2022, The P-and S-wave decomposition in a multicomponent elastic wavefield based on the divergence and curl operators and their applications in elastic reverse time migration: IEEE Transactions on Geoscience Remote Sensing, **60**, 1–13, doi: 10.1109/TGRS.2022.3224736.

Li, B., and A. Stovas, 2021, Decoupled approximation and separate extrapolation of P-and SV-waves in transversely isotropic media: Geophysics, **86**, no. 4, C133–C142, doi: 10.1190/geo2020-0232.1.

Liang, K., D. Cao, S. Sun, and X. Yin, 2023, Decoupled wave equation and forward modeling of qP wave in VTI media with the new acoustic approximation: Geophysics, **88**, no. 1, WA335–WA344, doi: 10.1190/geo2022-0292.1.

Liu, Q., J. Zhang, Y. Lu, H. Gao, S. Liu, and H. Zhang, 2019, Fast Poynting-vector based wave-mode separation and RTM in 2D elastic TI media: Journal of Computational Physics, **381**, 27–41, doi: 10.1016/j.jcp.2018.12.024.

Martin, G. S., K. J. Marfurt, and S. Larsen, 2002, Marmousi-2: An updated model for the investigation of AVO in structurally complex areas: 72nd Annual International Meeting, SEG, Expanded Abstracts, 1979–1982, doi: 10.1190/1.1817083.

McMechan, G. A., 1983, Migration by extrapolation of time-dependent boundary values: Geophysical Prospecting, **31**, 413–420, doi: 10.1111/j.1365-2478.1983.tb01060.x.

Shabelansky, A., A. Malcolm, M. Fehler, X. Shang, and W. Rodi, 2015, Source-independent full wavefield converted-phase elastic migration velocity analysis: Geophysical Journal International, **200**, 954–968, doi: 10.1093/gji/ggu450.

Shabelansky, A. H., A. Malcolm, and M. Fehler, 2017, Converted-wave seismic imaging: Amplitude-balancing source-independent imaging conditions: Geophysics, **82**, no. 2, S99–S109, doi: 10.1190/geo2015-0167.1.

Stovas, A., T. Alkhalifah, and U. bin Waheed, 2020, Pure P-and S-wave equations in transversely isotropic media: Geophysical Prospecting, **68**, 2762–2769, doi: 10.1111/1365-2478.13026.

Sun, R., J. Chow, and K.-J. Chen, 2001, Phase correction in separating P- and S-waves in elastic data: Geophysics, **66**, 1515–1518, doi: 10.1190/1.1487097.

Sun, R., and G. A. McMechan, 2001, Scalar reverse-time depth migration of prestack elastic seismic data: Geophysics, **66**, 1519–1527, doi: 10.1190/1.1487098.

Sun, R., G. A. McMechan, and H.-H. Chuang, 2011, Amplitude balancing in separating P- and S-waves in 2D and 3D elastic seismic data: Geophysics, **76**, no. 3, S103–S113, doi: 10.1190/1.3555529.

Sun, R., G. A. McMechan, C.-S. Lee, J. Chow, and C.-H. Chen, 2006, Prestack scalar reverse-time depth migration of 3D elastic seismic data: Geophysics, **71**, no. 5, S199–S207, doi: 10.1190/1.2227519.

Thomsen, L., 1986, Weak elastic anisotropy: Geophysics, **51**, 1954–1966, doi: 10.1190/1.1442051.

Tsvankin, I., 2012, Seismic signatures and analysis of reflection data in anisotropic media, 3rd ed.: SEG.

Wang, W., B. Hua, G. A. McMechan, and B. Duquet, 2018, P- and S-decomposition in anisotropic media with localized low-rank approximations: Geophysics, **83**, no. 1, C13–C26, doi: 10.1190/geo2017-0138.1.

Xiao, X., and W. S. Leaney, 2010, Local vertical seismic profiling (VSP) elastic reverse-time migration and migration resolution: Salt-flank imaging with transmitted P-to-S waves: Geophysics, **75**, no. 2, S35–S49, doi: 10.1190/1.3309460.

Xie, X.-B., and R.-S. Wu, 2005, Multicomponent prestack depth migration using the elastic screen method: Geophysics, **70**, no. 1, S30–S37, doi: 10.1190/1.1852787.

Xu, S., A. Stovas, T. Alkhalifah, and H. Mikada, 2020, New acoustic approximation for transversely isotropic media with a vertical symmetry axis: Geophysics, **85**, no. 1, C1–C12, doi: 10.1190/geo2019-0100.1.

Xu, S., and H. Zhou, 2014a, Accurate simulations of pure quasi-P-waves in complex anisotropic media: Geophysics, **79**, no. 6, T341–T348, doi: 10.1190/geo2014-0242.1.

Xu, S., and H. Zhou, 2014b, Pure quasi-P wave calculation in anisotropic media: 84th Annual International Meeting, SEG, Expanded Abstracts, 3887–3891, doi: 10.1190/segam2014-0291.1.

Yan, J., and P. Sava, 2008, Isotropic angle-domain elastic reverse-time migration: Geophysics, **73**, no. 6, S229–S239, doi: 10.1190/1.2981241.

Yan, J., and P. Sava, 2009a, Elastic wave-mode separation for VTI media: Geophysics, **74**, no. 5, WB19–WB32, doi: 10.1190/1.3184014.

Yan, J., and P. Sava, 2009b, 3D elastic wave mode separation for TTI media: 79th Annual International Meeting, SEG, Expanded Abstracts, 4294–4298, doi: 10.1190/1.3255066.

Yan, R., and X.-B. Xie, 2012, An angle-domain imaging condition for elastic reverse time migration and its application to angle gather extraction: Geophysics, **77**, no. 5, S105–S115, doi: 10.1190/geo2011-0455.1.

Yang, J., H. Zhang, Y. Zhao, and H. Zhu, 2019, Elastic wavefield separation in anisotropic media based on eigenform analysis and its application in reverse-time migration: Geophysical Journal International, **217**, 1290–1313, doi: 10.1093/gji/ggz085.

Yang, J., H. Zhu, W. Wang, Y. Zhao, and H. Zhang, 2018, Isotropic elastic reverse time migration using the phase- and amplitude-corrected vector P- and S-wavefields: Geophysics, **83**, no. 6, S489–S503, doi: 10.1190/geo2018-0023.1.

Yoon, K., and K. J. Marfurt, 2006, Reverse-time migration using the Poynting vector: Exploration Geophysics, **37**, 102–107, doi: 10.1071/EG06102.

Zhang, L., L. Liu, F. Niu, J. Zuo, D. Shuai, W. Jia, and Y. Zhao, 2022, A novel and efficient engine for P-/S-wave-mode vector decomposition for vertical transverse isotropic elastic reverse time migration: Geophysics, **87**, no. 4, S185–S207, doi: 10.1190/geo2021-0609.1.

Zhang, L., Y. Zhao, L. Liu, K. Chen, Y. Wang, and J. Zuo, 2023, A fast anisotropic decoupled operator of elastic wave propagation in the space domain for P-/S-wave-mode decomposition and angle calculation, with its application to elastic reverse time migration in a TI medium: Geophysics, **88**, no. 3, T151–T164, doi: 10.1190/geo2022-0477.1.

Zhang, Q., and G. A. McMechan, 2010, 2D and 3D elastic wavefield vector decomposition in the wavenumber domain for VTI media: Geophysics, **75**, no. 3, D13–D26, doi: 10.1190/1.3431045.

Zhang, W., and Y. Shi, 2019, Imaging conditions for elastic reverse time migration: Geophysics, **84**, no. 2, S95–S111, doi: 10.1190/geo2018-0197.1.

Zhang, Y., A. Stovas, and L. De Siena, 2024, Wavefield simulation and reverse time migration for acoustic TTI media: Geophysics, **89**, no. 2, C75–C87, doi: 10.1190/geo2023-0137.1.

Zhou, X., X. Chang, Y. Wang, and Z. Yao, 2019, Amplitude-preserving scalar PP and PS imaging condition for elastic reverse time migration based on a wavefield decoupling method: Geophysics, **84**, no. 3, S113–S125, doi: 10.1190/geo2017-0840.1.

Zhou, Y., and H. Wang, 2017, Efficient wave-mode separation in vertical transversely isotropic media: Geophysics, **82**, no. 2, C35–C47, doi: 10.1190/geo2016-0191.1.

Zuo, J., F. Niu, L. Liu, S. Da, H. Zhang, J. Yang, L. Zhang, and Y. Zhao, 2022, 3D anisotropic P-and S-mode wavefields separation in 3D elastic reverse-time migration: Surveys in Geophysics, **43**, 673–701, doi: 10.1007/s10712-021-09688-8.

Zuo, J., F. Niu, L. Zhang, L. Liu, H. Zhang, K. Chen, D. Shuai, J. Yang, and Y. Zhao, 2023, Elastic wavefield decomposition for reverse time migration in 3D TI media: Pure and Applied Geophysics, **180**, 3559–3585, doi: 10.1007/s00024-023-03325-8.

Biographies and photographs of the authors are not available.